This is a preprint, the final version is subject to change, of the American Mineralogist (MSA)
Cite as Authors (Year) Title. American Mineralogist, in press.
DOI: https://doi.org/10.2138/am-2019-6997

REVISION 1

Interdiffusion of major elements at 1 atmosphere between natural shoshonitic and rhyolitic melts

Diego Gonzalez-Garcia[1,2,*], Francesco Vetere[1,3], Harald Behrens[3], Maurizio Petrelli[1], Daniele Morgavi[1], Diego Perugini[1]

[1] *Dipartimento di Fisica e Geologia, Università degli Studi di Perugia, Piazza Universitá, 06123 Perugia, Italy.*

[2] *Dipartimento di Scienze della Terra, Università degli Studi di Torino. Via Valperga Caluso 35, 10125 Turin, Italy.*

[3] *Institut für Mineralogie, Leibniz Universität Hannover. Callinstrasse, 3, 30167 Hannover, Germany.*

*Corresponding author**:** Diego González-García

e-mail: diego.gonzalezgarcia@unito.it

Tel.: +39 011 670 5110

Fax: +39 011 091 5182

This is a preprint, the final version is subject to change, of the American Mineralogist (MSA)
Cite as Authors (Year) Title. American Mineralogist, in press.
DOI: https://doi.org/10.2138/am-2019-6997

Abstract

The diffusive mass exchange of eight major elements (Si, Ti, Al, Fe, Mg, Ca, Na and K) between natural, nominally dry shoshonitic and rhyolitic melts was studied at atmospheric pressure and temperatures between 1230 and 1413 °C using the diffusion couple method. For six elements, effective binary diffusion coefficients were calculated by means of a concentration-dependent method to obtain an internally consistent dataset. Among these components, the range in diffusivities is restricted, pointing to a coupling of their diffusive fluxes. We find that the calculated diffusivities fit well into the Arrhenius relation, with activation energies (E_a) ranging from 258 kJ/mol to 399 kJ/mol in rhyolitic (70 wt.% SiO_2) melt and from 294 to 426 kJ/mol in latitic melt (58 wt.% SiO_2). Ti shows the lowest E_a, while Si, Fe, Mg, Ca and K have a similar value. A strong linear correlation is observed between $log\ D_0$ and E_a, confirming the validity of the compensation law for this system. Uphill diffusion is observed in Al in the form of a concentration minimum in the rhyolitic side of the couple, (at ca. 69 wt.% SiO_2), and in Na indicated by a maximum in the shoshonitic side (ca. 59 wt.% SiO_2). Fe shows weak signs of uphill diffusion, possibly due to the contribution of ferric iron. The data presented here extend the database of previously published diffusivities in the shoshonite-rhyolite system (González-Garcia et al. 2017) towards the water-free end and allows us to better constrain the water-dependence of major element diffusion at very low water concentrations. Combining both datasets, we find that *log D* is proportional to the square root of water concentration for a range between 0 and 2 wt.% H_2O. These results are of particular interest in the study of mass transfer phenomena in alkaline volcanic systems.

Key words: chemical diffusion, major elements, alkaline melts, magma mixing, Vulcano Island

Introduction

Chemical diffusion in silicate melts is a primary process governing several kinetic phenomena in nature. Some magmatic processes that depend on diffusion are the growth and dissolution of minerals (e.g., Zhang et al. 1989; Liang 2003), interaction of magmas with xenoliths and country rocks (Watson, 1982), and the mass transfer rates during magma mixing events (Morgavi et al. 2016). To adequately describe and model these occurrences, the diffusion process must be accurately known. Although a significant volume of data is already available in the literature (for a detailed summary, see Zhang et al. 2010), the number of studies addressing melts of natural compositions and specific magmatic systems is still scarce. Among them, González-García et al. (2017, 2018) provided a database of major and trace element diffusion in the shoshonite-rhyolite system from Vulcano island (Aeolian archipelago, Tyrrhenian Sea, Italy), and other similar magmatic systems worldwide. In the Aeolian Islands, particularly in Lipari and Vulcano, three magmatic endmembers have been identified, such as shoshonite, latite and rhyolite, and the evidence of mixing between them is widespread (Vetere et al., 2015; Nicotra et al., 2018; Rossi et al., 2019, Bullock et al., 2019). The Vulcano system has been active in historical times, and enclaves, banded pumices and disequilibrium mineral textures are common (Gioncada et al. 2003, Nicotra et al., 2018). Diffusive fractionation models of major and trace elements can be used to gain knowledge on the timescales

involved in pre-eruptive mixing processes (Petrelli et al., 2006; Perugini et al., 2008, 2010), and new data could lead to the improvements such timescales with existing chronometers (Perugini et al., 2015), which would impact risk assessment in a populated volcanic archipelago.

In this work, we aim to complete the previously published internally consistent database by focusing on the interdiffusion of eight major elements (Si, Al, Ti, Fe, Mg, Ca, Na and K) occurring between nominally dry (ca. 0.02 wt.% H_2O) shoshonitic and rhyolitic melts at atmospheric pressure and different temperatures (1230-1413 ºC). Our main aim is to determine, where possible, the effective binary diffusion (EBD) coefficients and establishing their temperature dependence by the Arrhenius equations. In the EBD approach, diffusivities are obtained for the component of interest considering the remaining components as a single component. In consequence, the obtained data are of more restricted applicability and can only be applied to the studied compositions or those not differing strongly, but they are potentially more useful in the study of natural systems. Also, non-Fickian phenomena (e.g., uphill diffusion) cannot be addressed. The second aim of this work is to better constrain the dependence of major element diffusivity on water content for the shoshonite-rhyolite system by extending the previously published dataset (González-García et al. 2017) towards water-poor melts, given that strong diffusivity variations are expected in such low water contents. The results presented here have implications for the study of magmatic processes in natural environments in the shoshonite-rhyolite and similar systems.

Materials and methods

Starting materials and glass synthesis

Two compositionally distinct natural volcanic rocks from recent eruptions of the Vulcano system were used as end-members in the diffusion experiments. The least evolved (more mafic) composition is a shoshonite (Vetere et al. 2007; Davì et al. 2009) from the Vulcanello lava platform, emplaced in the eruption period ending at c.a. 1250 AD (Keller 1980; Arrighi et al. 2006; De Astis et al. 2006). The more evolved, silicic end-member was sampled at the Pietre Cotte lava flow, which was produced in the la Fossa eruption of 1739 AD (Keller, 1980; Frazzetta et al. 1983); it is represented by a high-K rhyolitic obsidian (Clocchiatti et al. 1994; De Astis et al. 1997, Piochi et al. 2009). These two end-members represent the most extreme compositions erupted in the Vulcano system in the last two millennia (De Astis et al. 2006).

Rock samples without alteration and contamination of enclaves were selected, cleaned with distilled water and finally ground in an agate mortar to produce a fine-grained powder. Homogenization of the two end-members was achieved through two cycles of melting at 1600ºC and atmospheric pressure for 4 hours, using a Nabertherm ® HT 04/17 furnace, followed by a rapid quench and re-crushing of the obtained glass. Powders were re-melted inside a $Pt_{80}Rh_{20}$ crucible (Morgavi et al. 2015) and then rapidly quenched. Quenching of the shoshonitic melt was achieved by pouring into a plate, while the rhyolite was freely cooled in air. Glasses were analyzed for major element composition (**Figure 1** and **Table 1**) by means of an electron microprobe.

The produced shoshonite and rhyolite glasses were drilled and cut into cylinders with a diameter of 16 mm and height between 6 and 8 mm. One end of each cylinder was

polished to produce a flat and smooth surface to perfectly pair the two selected compositions.

Experimental setup

Diffusion experiments were carried out using a diffusion couple technique (Baker, 1989; Baker, 1990; Nowak and Behrens, 1997). The produced glass cylinders from each end-member were placed inside a cylindrical alumina (Al_2O_3) crucible with an inner diameter of 16 mm, an outer diameter of 20 mm and height of 30 mm (**Figure 2**). The denser shoshonitic glass was placed at the bottom, and the rhyolitic at the top of the couple, in contact through their polished ends to avoid gravitational overturning.

Table 2 summarizes the experimental conditions. Runs were performed at ambient pressure and high temperature (1230 to 1413 ºC) inside a Nabertherm® furnace, with a run duration of 4 hours. Once the furnace reached the experimental temperature, the alumina crucible with the diffusion couple was placed inside the chamber. In addition to the furnace thermocouples, temperature was monitored using an in-house built S-type thermocouple ($Pt_{10}Rh_{90}$ vs. Pt) within an Al_2O_3 sheath, positioned ca. 0.5 cm above the sample. OMEGA wireless thermocouple transmitters UWTC-Series were employed (OMEGA Engineering, INC., Stamford, Connecticut, USA). Uncertainty on temperature measurements is on the order of ±0.5 K (Vetere et al., 2019). Once the experiment was finished, the furnace was opened, and the crucible was placed outside on a ceramic plate, carefully avoiding any shaking. Cooling to near-ambient temperature is achieved within few minutes, and cooling rates in higher than 250 K/min are achieved.

Analytical procedure

The experimental products (alumina crucible containing the diffusion couple glass) were cut longitudinally, and sections with a thickness of 150 μm were produced for analysis by electron microprobe (EPMA). Major element glass compositions were obtained by a Cameca SX-100 electron microprobe at the Institute of Mineralogy of the Leibnitz University of Hannover (Germany). Operating conditions were an accelerating potential of 15 kV, beam current of 4 nA and a defocused beam diameter of 10 μm to minimize alkali loss. Precision and accuracy were tested by measuring VG-568 (rhyolite) and VG-2 (basalt) reference glasses (Jarosewich et al. 1980; Helz et al. 2014). No evidence of alkali loss was observed during analyses. The analytical error varies from 1% for SiO_2 to 10 % for minor oxides. Two linear profiles centered at the interface with a length between 2 and 4 mm were measured for each experiment, taking care to avoid zones affected by bubble migration (see details reported below). The spacing between spots varied between 12 and 25 μm.

Moreover, in two of the experiments one additional profile was acquired across the alumina-glass interface, to check for the possible effect of aluminum diffusion from the refractory material to the studied glasses. Results show that contamination was limited to less than 500 μm in the shoshonite and less than 100 μm in the rhyolite.

Two of the experiments (AP-1 and AP-2) were also analyzed for water content by Fourier Transform Infrared spectroscopy (FTIR). The device used is a Bruker IFS88 spectrometer coupled with an IR-Scope II microscope (Institut für Mineralogie, Leibniz Universität Hannover). Spectra were acquired in the mid-infrared region (MIR) of the spectrum, in which the fundamental OH stretching vibration band at 3550 cm^{-1} is of

160 interest for quantification of the total water content. The amplitude of the band was
161 measured after subtraction of a linear baseline, and concentrations were calculated using
162 the modified Beer-Lambert law and mid-infrared absorbance of 67 $L \cdot mol^{-1} \cdot cm^{-1}$ as given
163 by Stolper (1982).

164 In order to constrain the oxidation state of Fe, small glass chips (<10 mg) from the two
165 ends of the diffusion couples were analysed by the wet-chemical colorimetric method
166 described by Schuessler et al. (2008). Fe^{2+}/Fe_{tot} ratio was determined by absorption
167 spectrometry in the visual spectrum using a Shimadzu UV 1800 UV/VIS spectrometer.
168 This method allows to determine the Fe^{2+}/Fe_{tot} ratios with high precision (typically within
169 < 3%).

170

171 **Evaluation of diffusion profiles**

172 Concentration-dependent, EBD coefficients were calculated form the concentration-
173 distance profiles using the modified Boltzmann-Matano method by Sauer and Freise
174 (1962), following a three-step procedure that comprises (1) normalization of the
175 compositional range, (2) fitting the analytical data by a polynomial function and (3)
176 calculation of the diffusion coefficients from the polynomial. The calculation was
177 implemented in a Python programming language script (Oliphant, 2007; González-Garcia
178 et al., 2018). The analytical solution for one-dimension molar volume independent
179 diffusion from Sauer and Freise (1962) was used:

180

181 $$D(x) = \frac{1}{-2t(\partial c/\partial x)}\left[(1-c(x))\int_x^{\infty} c\,dx + c(x)\int_{-\infty}^{x}\big(1-c(x)\big)dx\right] \quad (1)$$

182

where $c(x)$ is the normalized composition of the diffusing component. Boundary conditions are, $c(x) = 1$ at $x = -\infty$, and $c(x) = 0$ at $x = \infty$.

The application of the Sauer and Freise method results in a continuous variation of diffusion coefficients in the compositional space, assigning one diffusivity value to each point in the concentration-distance profile (see **Supplementary Table ii**). However, this results in artifacts in the extreme ends of the profile, where the diffusive slope tends to plateau. For this reason, diffusivities are given here for a range between 20 and 80% of the compositional interval between end-members. To make easier the comparison of data, diffusion coefficients of all six elements were extracted from the resulting data at four compositions corresponding to 20%, 40%, 60 % and 80% of the end-member compositional range, respectively corresponding to a latite (herein Lt_{58}), two trachytes (Tr_{62} and Tr_{66}) and a rhyolite (Rh_{70}). Subscripts represent the SiO_2 contents (details on this procedure are reported in González-García et al. (2017, 2018). End-member and intermediate compositions for all four experimental runs are listed in **Table 3**.

Results

Run products

An example of a section through an experimental product is given in **Figure 3a**. It is noteworthy to mention the prominent curvature of the melt-melt interface and the surface of the rhyolitic glass. This configuration is most probably due to wetting behaviour at the three-phase contact (alumina-melt-air) and is probably established at the beginning of the experiment. Due to the large diameter/thickness ratio of the couple cylinders, the central zone can be considered flat (**Figures 3b and 3c**). Water contents estimated from FTIR in

two of the experiments (AP-1 and AP-2) yielded average results of 0.021 ± 0.004 wt.% at the interface region (see **Table 4**). However, far from the interface rhyolitic melt increases to 0.030 wt.%, and shoshonite decreases to 0.013 wt.%. These values are one order of magnitude lower than those found in the nominally dry glasses from González-García et al. (2017), ca. 0.3 wt.%, using the same end-members in high-pressure diffusion couple experiments (see Discussion section). This difference is explained by hydrogen infiltration through capsule walls and subsequent reduction of Fe^{3+} in the high-pressure experiments, which were performed inside closed noble metal ($Au_{80}Pd_{20}$) capsules, as opposed to the open Al_2O_3 crucible used in this work that allows water to escape freely. All experimental glasses are crystal-free but show a small amount of bubbles concentrated in the interface and the rhyolitic sides. The rhyolite contains about 3 vol% of bubbles with variable sizes between 25 and 200 μm which originate from the synthesis using powder as starting materials. Additionally, bubbles are visible at the interface between shoshonite and rhyolite as well as at the interface between the melts and the crucible walls. These bubbles originate from trapped air which was enclosed during melting of glass cylinders. Considering the size of the bubbles and the high viscosity of the rhyolite melt, the bubbles are basically immobile on the time scale of the experiments. However, such bubbles may disturb chemical exchange between both melt bodies and, therefore, bubble-bearing areas were carefully avoided in profiling.

Effective experimental duration

Although nominal experimental times were 4 hours counted from the closure of the furnace after introducing the crucible, actual dwell time at the experimental temperature

is shorter due to the required heating-up times. Heat-up ramps measured at the start of the experiments allowed to define the "real dwell temperature" (**Table 2**). The thermal evolution of heat-up period indicates that experimental temperatures are achieved within 5 K approximately after 290 (run AP-4) to 380 seconds (run AP-1) after the closure of the furnace (**Figure 4**), less than 3% of the nominal run time. Effective experiment durations were calculated by assuming an Arrhenian behaviour of diffusivity during heat-up ramps and integrating the diffusivity as a function of T with respect to t during that interval (Zhang and Behrens 2000). Thus, the effective heating time (t_{eff}) can be calculated by the following expression (Koepke and Behrens 2001):

$$t_{eff} = \int \frac{D_{T(t)}}{D_{Texp}} dt = \int exp\left(\frac{E_a}{R} \cdot \left(\frac{1}{T(t)} - \frac{1}{T_{exp}}\right)\right) dt \quad (2)$$

where $D_{T(t)}$ is diffusivity as a function of temperature, which is itself a function of time, $T(t)$; D_{Texp} is the diffusivity at the experimental dwell temperature (T_{exp}); E_a is the activation energy and R the ideal gas constant.

The E_a values, given in **Table 5,** were used in the calculation. As expected for each experiment, activation energies vary along the diffusion profile, and as a consequence, the average of the listed values was used for a given element. Given the similarities of this value for all elements, we assumed 350 kJ/mol in our calculation, which is near the average of all of them. As a result, calculated effective heating times were in the order of 151 s (run AP-4) to 210 s (run AP-1). A variation of 50 kJ/mol in E_a results in a difference of <10 s in heating time. Final effective experiment durations are listed in **Table 2**. Given the way sample cooling was achieved, we cannot account for cooling timescales, but we assume it is much faster than heating and therefore its effects are negligible.

252

253 **Iron oxidation state**

254 Since experiments are performed in air, highly oxidizing conditions are expected.
255 Determination of the iron oxidation state (**Figure 5**) by a colorimetric wet-chemical
256 method (Schuessler et al. 2008) indicates that no significant variation can be observed
257 with increasing temperature. Fe^{2+}/Fe_{tot} ratios range from 0.33 to 0.37 for shoshonitic
258 glasses, and from 0.40 to 0.45 for rhyolitic glasses in the diffusion couples in the
259 temperature interval from 1230 to 1413 ºC. Using these Fe^{2+}/Fe_{tot} ratios, the Borisov et al.
260 (2018) model predicts oxygen fugacity (given as log fO_2/bar) ranging from -4.5 at 1230
261 ºC to -3.2 at 1413 ºC for shoshonitic melts and from -3.7 to -2.4 for rhyolitic melts, i.e.
262 approximately 2.0 to 2.5 log units below the magnetite-hematite oxygen buffer (MH).
263 Observed differences in log *fO2/bar* between the halves of the diffusion couples are <0.8
264 log units. Since diffusion experiments were performed at a temperature lower than the
265 synthesis temperature of 1600ºC (and therefore higher log fO_2), redox equilibrium in the
266 couples must be achieved by oxygen in-diffusion over several mm. This process is too
267 slow to change the ferric/ferrous iron ratio near the interface, and, hence, experiments are
268 performed at constant Fe^{2+}/Fe_{tot} rather than at constant oxygen fugacity. These variations
269 may have an impact on the derived Fe diffusivities.

270

271 **Diffusion data**

272 **Figure 6** shows an example of the concentration-distance profiles measured with the
273 EPMA. The complete dataset of EPMA concentration-distance profiles is reported as
274 **Supplementary Table i**. Eight of the major oxides (SiO_2, TiO_2, Al_2O_3, FeO_T, MgO,

CaO, Na_2O, and K_2O) are well resolved throughout the length of the profiles (FeO_T denotes total iron expressed as FeO). All oxides except Al_2O_3 and Na_2O show a normal diffusive behaviour, which can be explained by the Fick's laws of diffusion. Hence, an effective binary diffusion approach (EBD) is possible. However, it should be pointed out that diffusivities obtained using the EBD are only applicable to compositions and conditions studied here, and thus are not transferable to widely different compositional systems. In order to obtain a complete description of the interdiffusion in a multicomponent system, a diffusion matrix is required, but in practice such matrix can be constraint only in simpler systems (up to 8 components; Guo and Zhang, 2016, 2018) and needs a different experimental approach (e.g., Liang 2010); hence it is beyond the scope of this work.

Figure 6a shows concentrations recalculated to a compositional range from 0 to 1**,** highlighting the similarity of the concentration-distance profiles for all measured major oxides. Diffusion distances (that is, the length of the diffusive zone) are very similar for each element, and in turn, higher in the shoshonitic melt than in the rhyolitic one. The observed shapes also support the semi-infinite behaviour of each half of the couple, since diffusion has only affected their central section. Although very weak uphill diffusion is observed in FeO_T profiles (**Figure 6b**), since the deviation from normal diffusion behaviour is only small, Fe is included in the "normal diffusion group". It is noteworthy that the uphill diffusion of FeO_T profiles was not observed in the hydrous, HP experiments (González-García et al. 2017).

Table 4 summarizes the measured effective binary diffusion (Zhang 2010) coefficients of the six major elements (Si, Ti, Fe, Mg. Ca, and K) with "normal" diffusion

behavior, as obtained from the Sauer and Freise (1963) method, as outlined above. The complete set of diffusion coefficients is given in **Supplementary Table ii**. Diffusion coefficients have a small range of variation, as already inferred from the similarity of the concentration-distance profiles. Keeping a constant composition, variations in major element diffusivities are less than 0.3 log units (slightly above the estimated errors), clearly pointing to an extensive coupling between all major components. Comparing all data sets, Si tends to show the slowest diffusion, but the difference to other elements is small and usually within error. Within the compositional space, variations in diffusivity are clear and consistent. For a given element, diffusivities are 0.7 to 1 log unit faster in Lt_{58} compared to Rh_{70}. The applied modified Boltzmann-Matano method produces smooth and continuous variations in which *log D* decreases linearly with the SiO_2 content, and this relationship improves notably when considering the sum Si+Al in molar fractions. These findings agree with published results from quartz dissolution experiments in basalt and rhyolite (Yu et al., 2019). In fact, Si diffusivities obtained in this work can be modeled within ±0.7 log units by using their Si diffusion equation. In spite of showing slight uphill diffusion (**Figure 6**) and the variable Fe^{2+}/Fe_{tot} ratio, iron conforms to the remaining elements and shows a comparable behavior, as a consequence of diffusive coupling.

However, additional insights on Si and Al diffusion can be obtained by modeling the profiles measured in the alumina to melt interface in AP-3 and AP-4 experiments. Results are reported in **Supplementary Figure 1** and indicate that in the pure shoshonitic and rhyolitic melts, diffusion is up to 27 times faster in the shoshonite than in the rhyolite. These data are complementary to the concentration-dependent diffusivities and show that

Al diffusion in the absence of large compositional gradients is ca. 0.3 log units faster than Si.

Arrhenius parameters

The temperature dependence of the diffusion coefficients is expressed by the Arrhenius equation

$$D = D_0 e^{-Ea/RT} \qquad (3)$$

where D_0 is the pre-exponential factor (m^2/s), E_a is the activation energy (J/mol), R is the gas constant (J/mol K) and T is temperature (K). The Arrhenius parameters were calculated by linear fitting of the diffusion coefficients in a *1000/T vs. ln D* diagram (**Figure 7**).

Table 5 summarizes the Arrhenius parameters obtained by the linear fit, as represented in **Figure 7**. Calculated activation energies range from 269 ± 20 kJ/mol to 353 ± 27 kJ/mol for the Rh_{70} composition, and from 277 ± 62 kJ/mol to 366 ± 40 kJ/mol for Lt_{58}. E_a values are slightly larger for mafic compositions than silicic ones, but variations are similar, in magnitude, to the estimated error. The lowest E_a was derived for Ti, while Si, Fe, Mg, Ca and K display comparable values and within error of each other. It is also noteworthy to mention the very small E_a range in Fe across the compositional spectrum (374-399 kJ/mol), located also in the high-end of our E_a range. This is probably related to the change in redox state of iron with melt composition (**Figure 5**).

Discussion

The compensation law for diffusion in shoshonite-rhyolite melts

The compensation law is an empirical relation suggested by Winchell (1969), describing a log-linear correlation between the Arrhenius parameters D_0 and E_a. For diffusion in silicate melts that can be expressed as follows:

$$E_a = a + b \cdot logD_0 \qquad (4)$$

where E_a and D_0 are the Arrhenius parameters, and a and b are constants belonging to a particular melt composition. Various works have shown its validity for a variety of systems and components (e.g., Jambon 1982, Henderson et al. 1985, Koepke and Behrens 2001, Holycross and Watson 2016).

Data shown in **Figure 8** clearly emphasizes a linear relation between $log\ D_0$ and E_a for all four intermediate compositions, in all cases with a good correlation coefficient. The linear fits are parallel and shift towards higher E_a and $log\ D_0$ with increasing silica content, although this shift is within the error of the Arrhenius parameters. This means that, although the compensation law is not highly sensitive to bulk melt composition, a single compensation law cannot be used for the whole compositional range in our experiments. It is interesting to notice that there is no discrimination between network formers (mainly Si) and network modifiers (mainly Mg, Ca, Na and K, with Ti and Fe acting in both ways). This good correlation points to the prevalence of the already mentioned diffusive coupling in the compensation law and suggests that the same process (e.g. breaking and reformation of T-O bonds, with T being Si or Al) is controlling the motion of all melt constituents. However, it should be noted that studies with larger databases have found larger scatter (e.g. Brady and Cherniak, 2010), making necessary a careful examination of the compensation law for each case.

367 **Uphill diffusion**

368 As noted above, Al_2O_3 and Na_2O show effects of strong uphill diffusion, in the form
369 of a minimum in the rhyolitic side of the couples or a maximum in the shoshonitic side.
370 In addition, a weak minimum appears in the FeO_T profiles (**Figure 6 b-d**). However, no
371 accompanying maximum or minimum is observed in the opposite side of the interface of
372 the couple. This observation contrasts to uphill diffusion in simple synthetic systems
373 (with lower or absent compositional contrast), where both a minimum and a maximum
374 are observed to either side of the interface (e.g. Guo and Zhang 2016), and also to uphill
375 diffusion phenomena in trace elements in the shoshonite-rhyolite system (Gonzalez-
376 Garcia et al. 2018), where asymmetric maximum-minimum shapes are always observed.
377 This fact could be the consequence of faster diffusivity in the shoshonitic side for Al, and
378 in the rhyolitic side for Na, as highlighted by Zhang et al., (2010). This lack of maximum
379 in one side of the couple was also observed in systems with non-infinite behaviour of the
380 couple (Acosta-Vigil et al., 2002), but given the large size of our experiments (Figs. 2
381 and 3), this is probably not the case here. In systems with large bulk compositional
382 gradients, the existence of uphill diffusion is an indicator suggesting that elemental
383 activity gradients control diffusive fluxes.

384 Additional insights can be obtained by comparing the uphill diffusion profiles with
385 those obtained by González-García et al. (2017) in diffusion couples using identical end-
386 members but at high pressure and hydrous conditions. Uphill diffusion in Al_2O_3 and,
387 especially, Na_2O, is more prominently visible in the atmospheric pressure experiments
388 than in the high-pressure ones. Also, the weak minimum in the FeO_T profiles appears, a
389 feature that is absent in the FeO_T profiles from high-P experiments (González-Garcia et

al. 2017). Considering iron, the observed change could be produced by the more oxidizing conditions in the atmospheric pressure experiments, where the higher relative abundance of the slower diffusing Fe^{3+} may be responsible for the observed behavior. This is consistent with Fe^{3+} behaving mainly as a network former, similar to Al^{3+}, as opposed to the predominant role of Fe^{2+} as a network modifier (Mysen and Richet, 2005).

Dependence of diffusivities on viscosity

Some relations have been proposed to relate diffusivity and viscosity of melts. Possibly the most widely used of them is the Eyring equation (Glasstone et al., 1941), that relates diffusivity with viscosity, temperature and diffusive jump distance:

$$D = \frac{k_B \cdot T}{\lambda \cdot \eta} \quad (5)$$

where T is the temperature (K) k_B is the Boltzmann constant, λ is the interatomic jump distance and η is the melt viscosity ($Pa \cdot s$). The Eyring equation has been found to be of limited applicability tin the study of silicate melts (e.g. Zhang et al., 2010), and there are variable levels of agreement between the Eyring equation and observed diffusivities in particular conditions.

In order to be consistent with previous works (González-Garcia et al., 2017, 2018), a jump distance of 0.4 nm, roughly representing the value of atomic spacing in silicates (see also Fanara et al., 2017), was used to link viscosity and diffusivity. Melt viscosities were calculated by using the empirical viscosity model of Giordano et al. (2008). Calculated viscosities and Eyring diffusivities are listed in **Table 4. Figure 9** shows a comparison between measured diffusivities and calculated Eyring diffusivities for the different elements and the intermediate melt compositions. We observe that within each

melt composition, trends are parallel to the value given by the Eyring equation, but they progressively diverge from that value with increasing silica content. In Lt_{58} composition, diffusivities are ca. 0.1-0.5 log units higher than Eyring diffusivity, and the difference increases to 0.9-1.2 log units in Rh_{70}. In other words, the variation of diffusivity in the studied conditions is twofold: variation of temperature results in a log *D* variation concordant with the Eyring equation, while composition variation results in an increasing divergence from Eyring diffusivity with silica content (higher melt viscosities).

Implications for the dependence of diffusivity on water content

Data presented here allow to extend the hydrous diffusivity dataset (0.3-1.9 wt.% H_2O) obtained at high pressures (50-500 MPa), since we use the identical shoshonitic and rhyolitic end-members and intermediate compositions reported in González-García et al. (2017). Since pressure has only minor effect on diffusion in in silicate melts (Zhang et al., 2010) and the pressure range is relatively small, a direct comparison of the diffusivities obtained at both atmospheric and high-pressure conditions is possible. On the other hand, differences in iron redox state (notably more oxidizing conditions in the AP experiments relative to HP ones, see above) should not contribute significantly except in the case of iron. As already pointed out before, Fe^{2+}/Fe_{tot} ratios are lower for the 1 atmosphere experiments than for the HP experiments. In addition, in the HP experiments the iron oxidation state depends also on water content, since hydrogen fugacity is fixed. For iron, Fe^{3+} diffusion is expected to be significantly slower than that of Fe^{2+}, although existing data does not allow to quantify precisely this variation (Zhang et al. 2010). However, we do not expect a significant variation in Fe diffusivity due to the difference in oxygen

fugacity in the high-pressure vs atmospheric pressure experiments. **Figure 10** shows the Si atmospheric pressure diffusion data (corrected for a temperature of 1200ºC by using the Arrhenius equations obtained above) plotted along hydrous high-pressure diffusion. The complete set of diagrams for all elements is available as **Supplementary Figure 2**.

Diffusivities in AP experimental conditions, after temperature correction, are 0.6 to 0.8 orders of magnitude below those measured at HP and 0.3 wt. % H_2O. Such a difference is expected from viscosity studies in hydrous melts, where an important viscosity decrease is observed in the first 0.5 wt.% H_2O, followed by a small decrease at 2-2.5 wt. % H_2O (Richet et al. 1996; Dingwell et al. 1996). In contrast, the difference in Fe^{2+}/Fe_{tot} ratio between HP and AP experiments is not enough to influence viscosity significantly (Dingwell, 1991). Ti is apparently an exception showing only slight decrease in diffusivity relative to 0.3 wt.% H_2O in the most mafic compositions (**Supplementary Figure 2**), but this must be taken with caution given the large error associated with Ti diffusivities.

The best fit of the experimental data is obtained by considering a square root dependence on water concentration rather than a linear one, as suggested in Gonzalez-Garcia et al (2017), in the following form:

$$log\ D = a_0 + a_1 \cdot w^{0.5} \quad (6)$$

where w is the water content in wt. % and a_0 and a_1 are fitting parameters. For SiO_2, a_0 varies between -13.48 and -13.66, and a_1 varies between, and 1.31 and 1.11, for Lt_{58} and Rh_{70}, respectively, as reported in **Figure 10**. By using this approach, R^2 value is greater than 0.91. The inclusion of the new atmospheric pressure dataset extends this trend and provides a better fit of the data. The observed trends agree well with published trends at

459 higher water contents, where diffusivities as a function of water increase quickly in the
460 first 2-3 wt.% and become asymptotic for water concentrations higher than 4 wt.% H_2O
461 (e.g. Harrison and Watson 1983; Baker et al. 2002). The paucity of systematic data for
462 hydrous melts in the literature prevents a direct comparison with trends showed here, but
463 Zhang et al. (2010) noted proportionality between *ln D* and the square root of [H_2O] for
464 several trace elements (Y, La, Th, U). Harrison and Watson (1983) and Baker et al.
465 (2002) also observed similar behavior in Zr diffusion during zircon dissolution in
466 variably hydrous haplogranitic melts. Although this kind of relationship has been
467 suggested before, our dataset is the first where it has been consistently observed for a
468 wide group of components.

469 Recently, Yu et al (2019) suggested that the compositional dependence of Si
470 diffusivity could be related to Si+Al in mole fraction, including H in the calculation as a
471 cation. The authors find that the variations with H_2O could be due to a dilution effect of
472 Si+Al in the presence of H_2O. In our dataset, we find that diffusivities at 1% and 2% H_2O
473 tend to converge to the same trend when this procedure is applied, but the drier
474 experiments (0.02 and 0.3 wt.% H_2O) fall below this trend. This might be an indication
475 that at least part of the water effect could indeed be due to Si+Al dilution.

476

477 **Implications**

478 The data presented throughout this manuscript complements and expands the available
479 datasets, providing information on diffusive behavior and Arrhenius relations of major
480 elements in natural, complex multicomponent systems where large concentration
481 gradients are present. We observed a widespread coupling between diffusivities of

different elements that contrasts to diffusion data obtained in systems lacking large compositional gradients, where a higher spread in diffusivities is observed (e.g. Zhang 2010). This is in agreement with available data in similar systems (Watson 1982; Zhang et al. 1989) and points to complex interactions between melt components resulting in coupled diffusion fluxes. In addition, Rossi et al. (2017) observed a similar coupling concentration decay rates among major elements (except Na) in chaotic mixing experiments using the same end-members. In consequence, although more restricted in practical use, our data is potentially more useful in the study of natural magmatic systems.

Furthermore, our results improve the knowledge on water dependence of diffusion in the shoshonite-rhyolite system by extending the available dataset towards the dry end of the spectrum, where large variations are expected. González-García et al. (2017) already showed that in the restricted range from 0.3 to 1.9 wt.%, variations can be assumed linear, but this is no longer true in the range from essentially dry melts to 0.3 wt.%. Since natural melts are rarely dry, and most of the available dataset of diffusivities in natural melts are from dry experiments, our dataset contributes to close the gap between laboratory data and natural environments. A particular field of application of our new data is the study of the chemical exchange of magma mixing events. Here we show that in essentially dry melts (in the order of 0.02 wt.% H_2O), diffusivities of major elements are up to 2 orders of magnitude slower than those at ca. 2 wt.% H_2O. This difference can lead to an overestimate of diffusion derived timescales up to a factor of 100 if dry diffusivities are used instead of wet ones.

504 This is particularly useful to interpret dynamic mixing experiments where it is only
505 possible to work at atmospheric pressure (e.g. Morgavi et al. 2015, Rossi et al. 2017). An
506 interesting point comes from the basic observation that both temperature and water
507 content produce a significant increase in diffusivity, although in widely different ways.
508 Diffusivity is related to temperature by the Arrhenius equation (3), and to water content
509 by the square-root equation (6). Since some magma mixing laboratory experiments are
510 performed at room pressure and hence in essentially water-free melts, this could help to
511 approximate laboratory data to natural magma mixing examples, where the involved
512 melts are rarely dry. In principle, water content could be mimicked by increasing
513 experiment temperature by a certain amount, but these corrections would only be
514 approximate because of the different water dependence of each major element diffusivity,
515 and also because of differences in behavior produced by bulk chemistry.
516 Our data can also aid the interpretation of the chemical trends observed in mixed
517 volcanic and plutonic. Here we observe that Na and Al (and to a minor extent, Fe) can
518 fractionate towards one of the melts by the effect of uphill diffusion, leading to strongly
519 nonlinear correlations to other major elements. Such correlations have been observed in
520 nature (Weidendofer et al. 2014; Morgavi et al. 2016). Moreover, given the apparent
521 increase in compositional variability produced by elements diffusing uphill in the early
522 stages of mixing (González-Garcia et al. 2018), some caution is needed in the use of Na
523 and Al to obtain timescales based on concentration variance.
524 Our results are likely to be of interest in the study of volcanic systems where similar
525 melts are known to interact. In Vulcano, the last millennium of activity has produced
526 magmas from shoshonitic and latitic to rhyolitic compositions, and at lest the latter two

527 are known to interact in the shallow volcanic system (Vetere et al., 2015, Rossi et al.,
528 2019, Bullock et al., 2019, Nicotra et al, 2018). In fact, combining chemical compositions
529 of banded pumices and mixing experiments using latite and rhyolite as end-members
530 suggest mixing timescales in the order of tens of hours (Rossi et al., 2019) for recent
531 eruptions at Vulcano.
532

533 **Acknowledgements**

534 This research was funded by the European Research Council (ERC) Consolidator
535 Grant ERC-2013-CoG No. 612776 – CHRONOS to D. Perugini and by the MIUR-
536 DAAD Joint Mobility Project (grant number 57262582) to F. Vetere and H. Behrens. An
537 Alexander von Humboldt Foundation Senior Research Grant to F. Vetere is also
538 acknowledged. The help provided by Chao Zhang and Renat Almeev during microprobe
539 analysis at the University of Hannover is recognised, as well as Youxue Zhang and an
540 anonymous reviewer for their constructive review of the initial manuscript.
541

542 **References**

543 Acosta-Vigil, A., London, DE., Dewers, T.A., and Morgan VI, G.B. (2002) Dissolution
544 of corundum and andalusite in H_2O-saturated haplogranitic melts at 800ºC and 200
545 MPa: Constraints on Diffusivities and the Generation of Peraluminous melts.
546 Journal of Petrology, 43 (10), 1885-1908.

547 Arrighi, S., Tanguy, J.C., and Rosi, M. (2006) Eruptions in the last 2200 years at Vulcano
548 and Vulcanello (Aeolian Islands, Italy) dated by high-accuracy archeomagnetism.

549 Physics of the Earth and Planetary Interiors, 159, 225-233. DOI:
550 10.1016/j.pepi.2006.07.010

551 Baker, D.R. (1989) Tracer versus trace element diffusion: diffusional decoupling of Sr
552 concentration from Sr isotope composition. Geochimica et. Cosmochimica. Acta,
553 53, 3015–3023.

554 Baker, D.R. (1990) Chemical interdiffusion of dacite and rhyolite: anhydrous
555 measurements at 1 atm and 10 kbar, application of transition state theory, and
556 diffusion in zoned magma chambers. Contributions to Mineralogy and Petrology,
557 104, 407-433.

558 Baker, D.R., Conte, A.M., Freda, C. and Ottolini, L. (2002) The effect of halogens on Zr
559 diffusion and zircon dissolution in hydrous metaluminous granitic melts.
560 Contributions to Mineralogy and Petrology 142, 666-678. DOI: 10.1007/s00410-
561 001-0328-3

562 Borisov, A., Behrens, H., and Holtz, F. (2018) Ferric/ferrous iron ratio in silicate melts: a
563 new model for 1 atm data with special emphasis on the effects of melt composition.
564 Contributions to Mineralogy and Petrology, 173:98.

565 Brady, J.B., and Cherniak, D.J. (2010) Diffusion in minerals: an overview of published
566 experimental diffusion data. Reviews in Mineralogy and Geochemistry, 72, 899-
567 920.

568 Bullock, L.A., Gertisser, R.A., O'Driscoll, B., and Harland, S. (2019) Magmatic
569 evolution and textural development of the 1739 CE Pietre Cotte lava flow,
570 Vulcano, Italy. Journal of Volcanology and Geothermal Research, 372, 1-23.

571 Clocchiatti, R., Del Moro, A., Gioncada, A., Joron, J.L., Mosbah, M., Pinarelli, L., and
572 Sbrana, A. (1994) Assessment of a shallow magmatic system: the 1888-90
573 eruption, Vulcano Island, Italy. Bulletin of Volcanology, 56, 466-486.

574 Davì, M., de Rosa, R., Donato, P., Vetere, F., Barca, D., and Cavallo, A. (2009)
575 Magmatic evolution and plumbing system of ring-fault volcanism: the Vulcanello
576 peninsula (Aeolian islands, Italy). European Journal of Mineralogy, 21, 1009-1028.
577 doi: 10.1127/0935-1221/2009/0021-1955

578 De Astis, G., La Volpe, L., Peccerillo, A., and Civetta, L. (1997) Volcanological and
579 petrological evolution of Vulcano island (Aeolian Arc, southern Thyrrhenian sea).
580 Journal of Geophysical Research-Solid Earth, 102, 8021-8050.

581 De Astis, G., Dellino, P., La Volpe, L., Lucchi, F., and Tranne, C.A. (2006) Geological
582 map of the island of Vulcano (Aeolian Islands). University of Bari, University of
583 Bologna and INGV. LAC, Florence.

584 Dingwell, D.B. (1991) Redox viscometry of some Fe-Bearing silicate melts. American
585 Mineralogist, 76, 1560-1562.

586 Dingwell, D.B., Romano, C., and Hess, K.-U. (1996) The effect of water on the viscosity
587 of a haplogranitic melt under P-T-X conditions relevant to silicic volcanism.
588 Contributions to Mineralogy and Petrology, 124, 19-28.

589 Fanara, S., Sengupta, S., Becker, H.-W., Rogalla., D., and Chakraborty, S. (2017).
590 Diffusion across the glass transition in silicate melts: Systematic correlations, new
591 experimental data for Sr and Ba in calcium-aluminosilicate glasses and general
592 mechanisms of ionic transport. Journal of Non-Crystalline Solids, 455, 6-16.

593 Frazzetta, G., La Volpe, L., and Sheridan, M.F. (1983) Evolution of the Fossa cone.
594 Journal of Volcanology Geothermal Research, 17, 329-360.

595 Gioncada. A., Mazzuoli, R., Bisson, M., and Pareschi, M.T. (2003) Petrology of volcanic
596 products younger than 42 ka on the Lipari-Vulcano system (Aeolian Islands, Italy):
597 an example of volcanism controlled by tectonics. Journal of Volcanology and
598 Geothermal Research, 145, 91-118.

599 Giordano, D., Russell, J.K., and Dingwell, D.B. (2008) Viscosity of magmatic liquids: a
600 model. Earth and Planetary Science Letters, 271, 123-134.

601 Glasstone, S., Laider, K.J., and Eyring, H. (1941) The Theory of Rate Processes, 611 p.
602 McGraw-Hill, New York.

603 González-García, D., Behrens, H., Petrelli, M., Vetere, F., Morgavi, D., Zhang, C., and
604 Perugini, D. (2017) Water-enhanced interdiffusion of major elements between
605 natural shoshonite and high-K rhyolite melts. Chemical Geology, 466, 86-101.

606 González-García, D., Petrelli, M., Behrens, H., Vetere, F., Fischer, L.A., Morgavi, D.,
607 and Perugini, D. (2018) Diffusive exchange of trace elements between alkaline
608 melts: Implications for element fractionation and timescale estimations during
609 magma mixing. Geochimica et Cosmochimica Acta, 233, 95-114.

610 Guo, C., and Zhang, Y. (2016) Multicomponent diffusion in silicate melts: SiO_2-TiO_2-
611 Al_2O_3-MgO-CaO-Na_2O-K_2O system. Geochimica et Cosmochimica Acta, 195,
612 126-141.

613 Guo, C., and Zhang, Y. (2018) Multicomponent diffusion in basaltic melts at 1350 ºC.
614 Geochimica et Cosmochimica Acta, 228, 190-204.

615 Harrison, T.M., and Watson, E.B. (1983) Kinetics of Zircon dissolution and zirconium
616 diffusion in granitic melts of variable water content. Contributions to Mineralogy
617 and Petrology, 84, 66-72.

618 Helz, R.T., Clague, D.A., Mastin, L.G., and Rose, T.R. (2014) Electron microprobe
619 analyses of glasses from Kilauea Tephra Units, Kilauea Volcano, Hawaii. U.S.
620 Geological Survey Open-File Report 2014-1090, 24 p. doi:10.3133/ofr20141090

621 Henderson, P., Nolan, J., Cunningham, G.C., and Lowry, R.K. (1985). Structural controls
622 and mechanisms of diffusion in natural silicate melts. Contributions to Mineralogy
623 and Petrology, 89, 263-272.

624 Holycross, M.E., and Watson, E.B. (2016) Diffusive fractionation of trace elements in
625 basaltic melt. Contributions to Mineralogy and Petrology, 171:80.

626 Jambon, A. (1982) Tracer diffusion in granitic melts: experimental results for Na, K, Rb,
627 Cs, Ca, Sr, Ba, Ce, Eu, to 1300 °C and a model of calculation. Journal of
628 Geophysical Research, 87, 797–810.

629 Jarosewich, E., Nele, J.A., and Norberg, J.A. (1980) Reference samples for Electron
630 Microprobe Analysis. Geostandards Newsletter, 4, 43-47.

631 Keller, J. (1980) The island of Vulcano. Rendiconti della Società Italiana di Mineralogia
632 e Petrologia, 36, 369–414.

633 Koepke, J., and Behrens, H. (2001) Trace element diffusion in andesitic melts: An
634 application of synchrotron X-ray fluoresecence analysis. Geochimica et
635 Cosmochimica Acta, 65 (9), 1481-1498.

636 Koyaguchi, T. (1989) Chemical gradient at diffusive interfaces in magma chambers.
637 Contributions to Mineralogy and Petrology, 103, 143-152.

638 Liang, Y. (2003) Kinetics of crystal-melt reaction in partially molten silicates: 1. Grain
639 scale processes. Geochemistry, Geophysics, Geosystems 4, 1045.

640 Liang, Y. (2010) Multicomponent diffusion in molten silicates: theory, experiments and
641 geological applications. Reviews in Mineralogy and Geochemistry, 72, 409-446.

642 Morgavi, D., Petrelli, M., Vetere, F.P., González-García, D., and Perugini, D. (2015)
643 High-temperature apparatus for chaotic mixing of natural silicate melts. Review of
644 Scientific Instruments, 86, 105108.

645 Morgavi, D., Arzilli, F., Pritchard, C., Perugini, D., Mancini, L., Larson, P., and
646 Dingwell, D.B. (2016) The Grizzly Lake complex (Yellowstone Volcano, USA):
647 Mixing between basalt and rhyolite unravelled by microanalysis and X-ray
648 microtomography. Lithos, 260, 457-474.

649 Mysen, B. O., and Richet, P. (2005) Silicate Glasses and Melts: Properties and Structure.
650 560 p. Elsevier, Amsterdam.

Nicotra, E., Giuffrida, M., Viccaro, M., Donato, P., D'Oriano, C., Paonita, A., and De Rosa, R. (2018) Timescales of pre-eruptive magmatic processes at Vulcano (Aeolian Islands, Italy) during the last 1000 years. Lithos, 316-317, 347-365.

Nowak, M., Behrens, H. (1997). An experimental investigation on diffusion of water in haplogranitic melts. Contributions to Mineralogy and Petrology, 126, 365–376.Oliphant, T.E. (2007) Python for scientific computing. Computing in Science and Engineering, 9, 10-20.

Oliphant, T.E. (2007). Python for scientific computing- Computing in Science and Engineering, 9, 10-20.

Perugini, D., De Campos, C., Dingwell, D.B., Petrelli, M., and Poli, G. (2008) Trace element mobility during magma mixing: Preliminary experimental results. Chemical Geology, 256 (3-4), 146-157.

Perugini, D., De Campos, C., Petrelli, M., and Dingwell, D.B. (2015) Concentration variance decay during magma mixing: a volcanic chronometer. Scientific Reports, 5, 14225.

Perugini, D., Poli, G., Perelli, M., De Campos, C.P., and Dingwell, D.B. (2010) Time-scales of recent Phlegrean fields eruptions inferred from the application of a 'diffusive fractionation' model of trace elements. Bulletin of Volcanology, 72, 431-447.

Petrelli, M., Perugini, D., and Poli, G. (2006) Time-scales of hybridisation of magmatic enclaves in regular and chaotic flow fields: petrologic and volcanologic implications. Bulletin of Volcanology. 68, 285-293.

Piochi, M., De Astis, G., Petrelli, M., Ventura, G., Sulpizio, R., and Zanetti, A. (2009) Constraining the recent plumbing system of Vulcano (Aeolian Arc, Italy) by textural, petrological and fractal analysis: the 1739 A.D. Pietre Cotte lava flow. Geochemistry, Geophysics, Geosystems, 10, 1-28.

Richet, P., Lejeune, A.-M., Holtz, F., and Roux, J. (1996) Water and the viscosity of andesite melts. Chemical Geology, 128, 185-197.

Rossi, S., Petrelli, M., Morgavi, D., González-García, D., Fischer, L.A., Vetere, F., and Perugini, D. (2017) Exponential decay of concentration variance during magma mixing: Robustness of a volcanic geochronometer and implications for the homogenization of chemical heterogeneities in magmatic systems. Lithos, 286-287, 396-407.

Rossi, S., Petrelli, M., Morgavi, D., Vetere, F.P., Almeev, R.R., Astbury, R.L., and Perugini, D. (2019) Role of magma mixing in the pre-eruptive dynamics of the Aeolian Islands volcanoes (southern Tyrrhenian Sea, Italy). Lithos, 324-325, 165-179.

Sauer, F., and Freise, V. (1962) Diffusion in binären Gemischen mit Volumenanderung. Zeitschrift für Elektrochemie und Angewandte Physikalische Chemie, 66, 353-363 (in German).

691 Schuessler, J.A., Botcharnikov, R.E., Behrens, H., Misiti, V. and Freda, C. (2008)
692 Oxidation state of iron in phono-tephritic melts. American Mineralogist, 93 (10),
693 1493-1504.

694 Stolper, E. (1982) Water in silicate glasses: an infrared spectroscopic study.
695 Contributions to Mineralogy and Petrology, 81, 1-17.

696 Vetere, F., Behrens, H., Misiti, V., Ventura, G., Holtz, F., De Rosa, R., and Deubener, J.,
697 (2007) The viscosity of shoshonitic melts (Vulcanello Penunsula, Aeolian Islands,
698 Italy): Insight on the magma ascent in dikes. Chemical Geology, 245, 89-102.

699 Vetere, F., Murri, M., Alvaro, M., Domeneghetti, M.C., Rossi, S., Pisello, A., Perugini,
700 D., and Holtz, F. (2019) Viscosity of Pyroxenite Melt and its Evolution during
701 Cooling. Journal of Geophysical Research: Planets, *in press*.

702 Vetere, F., Petrelli, M., Morgavi, D., and Perugini, D. (2015). Dynamics and time
703 evolution of a shallow plumbing system: The 1739 and 1888 eruptions, Vulcano
704 Island, Italy. Journal of Volcanology and Geothermal Research, 306, 74-82.

705 Watson, E.B. (1982) Basalt contamination by continental crust: some experiments and
706 models. Contributions to Mineralogy and Petrology, 80, 73-87.

707 Weidendorfer. D., Mattson, H.B., and Ulmer, P. (2014). Dynamics of magma mixing in
708 partially crystallized magma chambers: textural and petrological constraints from
709 the basal complex of the Austurhorn intrusion (SE Iceland). Journal of Petrology,
710 55 (9), 1865-1903.

711 Winchell, P. (1969) The compensation law for diffusion in silicates. High Temperature
712 Science, 1, 200-215.

713 Yu, Y., Zhang, Y., and Yang, Y. (2019) Kinetics of quartz dissolution in natural silicate
714 melts and dependence of SiO_2 diffusivity on melt composition. ACS Earth Space
715 Chem., 3 ()4), 599-616.

716 Zhang, Y. (2010) Diffusion in Minerals and Melts: Theoretical Background. Reviews in
717 Mineralogy and Geochemistry, 72, 5-59.

718 Zhang, Y. and Behrens, H. (2000). H_2O diffusion in rhyolitic melts and glasses. Chemical
719 Geology, 169, 243-262.

720 Zhang, Y., Walker, D. and Lesher, C. (1989). Diffusive crystal dissolution. Contributions
721 to Mineralogy and Petrology, 102, 492-513.

722 Zhang, Y., Ni, H., and Chen, Y. (2010) Diffusion data in silicate melts. Reviews in
723 Mineralogy and Geochemistry, 72, 311-408.

724

725 **Table captions**

726

727 **Table 1**. Composition of end-members, normalized to a water-free basis. Iron is given
728 as total ferrous iron oxide (FeO_T). End-member data are the average composition based
729 on 10 microprobe data points measured on the starting materials melted in air.

730

731 **Table 2**. Run conditions of the diffusion couple experiments and estimated effective
732 dwell times.

733

734 **Table 3**. Compositions of the rhyolitic (Rhy) and shoshonitic (Sho) ends of the
735 concentration-distance profiles and the intermediate compositions where diffusivities are
736 extracted, for all four experiments. End-member compositions are the average of the
737 extreme 5 points of each profile. Distance from the interface for each composition is also
738 listed.

739

740 **Table 4**. Diffusion coefficients calculated using the Sauer and Freise (1963) modified
741 Bolztmann-Matano method.

742

743 **Table 5**. Arrhenius parameters of major elements obtained by linear fitting of *1/T* vs *ln*
744 *D* plots.

745

746

747 **Figure captions**

748

749 **Figure 1**. Total alkali versus silica diagram, showing the end-member compositions as
750 well as the four intermediate compositions where diffusivities were extracted.

751

752 **Figure 2**: Sketch showing the experimental setup and dimensions of the crucible and
753 glasses.

754

755 **Figure 3**: Example of experimental product. (a) Image mosaic of a 300 μm thick
756 section of a diffusion couple (run AP-1), with dark shoshonite glass in the bottom and
757 light rhyolite on top. (b) and (c) EPMA back-scattered electron (BSE) images of the
758 interface are of two experiments (run AP-1 and run AP-3, respectively). The local
759 disturbances associated to bubbles were avoided during analyses.

760

761 **Figure 4**: Heat-up ramps as measured by a thermocouple located ca. 0.5 cm cm above
762 the crucible.

763

764 **Figure 5**: Iron oxidation state measured by a wet-chemical method (Schuessler et al.,
765 2008) from far-field end-member glasses in the diffusion experiments.

766

767 **Figure 6**: Concentration-distance profiles for (a) major element oxides with normal
768 diffusion profiles, with concentrations of individual oxides recalculated to a range of 0 to
769 1; (b) FeO_T profile alone, showing very weak uphill diffusion (see inset); (c) Al_2O_3, and
770 (d) Na_2O, showing the effects of prominent uphill diffusion. Data from experiment AP-3
771 (1274 ºC).

772

773 **Figure 7**. Arrhenius relationships of the six analyzed major elements.

774

775 **Figure 8**. Compensation law for major element diffusion.

776

777 **Figure 9.** Measured diffusion coefficients plotted against Eyring diffusivities
778 calculated from equation (5).

779

780 **Figure 10.** Water versus Si diffusivity diagram combining data at atmospheric
781 pressure (this work) and high pressure (González-García et al., 2017). The atmospheric
782 data has been corrected for temperature by using the Arrhenius equation **(Table 4**). The
783 full set of diagrams is available in the **Supplementary Materials**.

This is a preprint, the final version is subject to change, of the American Mineralogist (MSA)
Cite as Authors (Year) Title. American Mineralogist, in press.
DOI: https://doi.org/10.2138/am-2019-6997

Table 1

	Shoshonite		Rhyolite	
	wt.%	*σ*	wt.%	*σ*
SiO_2	53.34	±*0.77*	73.20	±*0.67*
TiO_2	0.69	±*0.04*	0.11	±*0.03*
Al_2O_3	16.42	±*0.15*	13.84	±*0.31*
FeO_T	8.14	±*0.28*	2.14	±*0.26*
MnO	0.21	±*0.13*	0.08	±*0.09*
MgO	4.64	±*0.10*	0.18	±*0.04*
CaO	8.04	±*0.18*	0.92	±*0.18*
Na_2O	5.46	±*0.21*	4.22	±*0.20*
K_2O	3.05	±*0.07*	5.31	±*0.06*

This is a preprint, the final version is subject to change, of the American Mineralogist (MSA)
Cite as Authors (Year) Title. American Mineralogist, in press.
DOI: https://doi.org/10.2138/am-2019-6997

Table 2

Run	T (ºC)	σ	Effective heatup time (s)	Eff. Duration (s)
AP-1	1230	±3	210	14230
AP-2	1322	±3	161	14241
AP-3	1274	±3	186	14226
AP-4	1413	±3	151	14261

This is a preprint, the final version is subject to change, of the American Mineralogist (MSA)
Cite as Authors (Year) Title. American Mineralogist, in press.
DOI: https://doi.org/10.2138/am-2019-6997

Table 4

Run		AP1	σ	AP3	σ	AP2	σ	AP4	σ
H_2O (wt%)[1]		0.021	±*0.004*			0.021	±*0.004*		
T (K)		1503	±*3*	1547	±*3*	1595	±*3*	1683	±*3*
Number of profiles		1		2		2		1	
Lt_{58} (Latite)									
log η (η in Pa s)[a]		2.81		2.51		2.21		1.7	
lod D (Eyring)[b]		-13.10		-12.78		-12.47		-11.94	
log D (D in m^2/s)	Si	-13.05	±*0.16*	-12.60	±*0.13*	-12.21	±*0.08*	-11.52	±*0.11*
	Ti	-12.76	±*0.21*	-12.57	±*0.16*	-12.04	±*0.15*	-11.70	±*0.19*
	Fe	-12.83	±*0.16*	-12.33	±*0.14*	-12.05	±*0.15*	-11.38	±*0.18*
	Mg	-12.91	±*0.09*	-12.46	±*0.11*	-12.02	±*0.09*	-11.56	±*0.14*
	Ca	-12.92	±*0.18*	-12.58	±*0.11*	-12.14	±*0.08*	-11.53	±*0.15*
	K	-13.02	±*0.17*	-12.54	±*0.09*	-12.25	±*0.13*	-11.39	±*0.12*
Tr_{62} (Trachyte)									
log η (η in Pa s)[a]		3.28		2.98		2.67		2.15	
lod D (Eyring)[b]		-13.57		-13.25		-12.93		-12.39	
log D (D in m^2/s)	Si	-13.35	±*0.15*	-12.87	±*0.13*	-12.68	±*0.13*	-12.00	±*0.11*
	Ti	-13.00	±*0.20*	-12.79	±*0.16*	-12.36	±*0.17*	-12.01	±*0.19*
	Fe	-13.19	±*0.20*	-12.60	±*0.14*	-12.40	±*0.17*	-11.72	±*0.18*
	Mg	-13.16	±*0.10*	-12.83	±*0.11*	-12.40	±*0.12*	-12.01	±*0.14*
	Ca	-13.19	±*0.13*	-12.80	±*0.11*	-12.48	±*0.10*	-11.94	±*0.15*
	K	-13.27	±*0.13*	-12.76	±*0.09*	-12.54	±*0.13*	-11.74	±*0.12*
Tr_{66} (Trachyte)									
log η (η in Pa s)[a]		3.74		3.43		3.2		2.58	
lod D (Eyring)[b]		-14.03		-13.70		-13.46		-12.82	
log D (D in m^2/s)	Si	-13.48	±*0.13*	-12.99	±*0.13*	-12.90	±*0.15*	-12.22	±*0.11*
	Ti	-13.13	±*0.18*	-12.87	±*0.16*	-12.56	±*0.13*	-12.17	±*0.19*
	Fe	-13.35	±*0.18*	-12.80	±*0.14*	-12.58	±*0.15*	-11.87	±*0.18*
	Mg	-13.31	±*0.10*	-13.01	±*0.11*	-12.58	±*0.11*	-12.16	±*0.14*
	Ca	-13.32	±*0.11*	-12.91	±*0.11*	-12.68	±*0.10*	-12.16	±*0.15*
	K	-13.40	±*0.11*	-12.91	±*0.09*	-12.72	±*0.13*	-11.94	±*0.12*
Rh_{70} (Rhyolite)									
log η (η in Pa s)[a]		4.2		3.88		3.56		3.01	
lod D (Eyring)[b]		-14.49		-14.15		-13.82		-13.25	
log D (D in m^2/s)	Si	-13.63	±*0.11*	-13.11	±*0.13*	-13.03	±*0.12*	-12.41	±*0.11*
	Ti	-13.28	±*0.18*	-12.93	±*0.16*	-12.70	±*0.13*	-12.33	±*0.19*
	Fe	-13.52	±*0.15*	-13.01	±*0.14*	-12.70	±*0.10*	-11.98	±*0.18*
	Mg	-13.47	±*0.10*	-13.10	±*0.11*	-12.71	±*0.09*	-12.32	±*0.14*
	Ca	-13.48	±*0.09*	-13.00	±*0.11*	-12.82	±*0.08*	-12.35	±*0.15*
	K	-13.57	±*0.09*	-13.05	±*0.09*	-12.85	±*0.13*	-12.12	±*0.12*

[a] *Dry melt viscosity as calcutated with the general viscosity model of Giordano (2008)*

[b] Eyring diffusivities calculated following eq. (5), assuming a jump distance of 0.4 nm.

This is a preprint, the final version is subject to change, of the American Mineralogist (MSA)
Cite as Authors (Year) Title. American Mineralogist, in press.
DOI: https://doi.org/10.2138/am-2019-6997

Table 5

Component	$\ln D_0$ (m^2/s)	σ	E_a (kJ/mol)	σ	R^2 of fit
			Lt_{58}		
Si	2.32	±0.71	404	±28	0.999
Ti	-5.95	±2.86	294	±38	0.984
Fe	-0.55	±1.89	375	±48	0.992
Mg	-0.88	±2.38	359	±31	0.978
Ca	0.23	±0.90	375	±27	0.997
K	4.12	±1.92	426	±33	0.994
			Tr_{62}		
Si	-2.98	±1.95	346	±39	0.986
Ti	-8.00	±2.61	274	±34	0.975
Fe	-0.27	±3.26	374	±48	0.976
Mg	-5.49	±2.38	309	±36	0.979
Ca	-3.87	±1.13	330	±36	0.996
K	1.13	±2.55	395	±33	0.961
			Tr_{66}		
Si	-5.50	±2.98	318	±39	0.966
Ti	-9.60	±3.06	258	±41	0.994
Fe	-0.34	±2.63	378	±48	0.985
Mg	-5.65	±1.99	312	±38	0.985
Ca	-6.41	±1.70	302	±36	0.990
K	-0.91	±2.75	374	±33	0.983
			Rh_{70}		
Si	-6.81	±2.98	305	±39	0.958
Ti	-10.58	±3.10	258	±39	0.985
Fe	0.90	±1.61	399	±38	0.995
Mg	-6.45	±2.44	305	±33	0.977
Ca	-7.99	±2.75	286	±30	0.970
K	-1.34	±2.67	372	±31	0.984

This is a preprint, the final version is subject to change, of the American Mineralogist (MSA)
Cite as Authors (Year) Title. American Mineralogist, in press.
DOI: https://doi.org/10.2138/am-2019-6997

Table 3

	Rhy	Rh_{70}	Tr_{66}	Tr_{62}	Lt_{58}	Sho
Experiment AP-1						
x (μm)	-262	-12	9	21	42	691
SiO_2	72.91	70.35	66.09	61.93	58.06	53.76
TiO_2	0.12	0.19	0.29	0.46	0.57	0.71
Al_2O_3	13.77	13.14	14.09	14.90	15.85	16.21
FeO_T	2.25	2.96	4.23	5.60	6.91	8.48
MgO	0.25	1.17	1.87	2.73	3.26	4.48
CaO	0.86	1.84	3.12	4.77	6.23	8.01
Na_2O	4.57	5.15	5.54	5.23	5.40	5.26
K_2O	5.26	5.20	4.77	4.38	3.72	3.08
Experiment AP-2						
x (μm)	-565	-48	8	48	129	1371
SiO_2	72.97	70.13	66.11	62.09	58.17	53.76
TiO_2	0.11	0.16	0.27	0.41	0.56	0.73
Al_2O_3	13.88	13.83	14.68	15.13	15.81	16.11
FeO_T	2.24	2.69	4.24	5.25	6.50	8.44
MgO	0.27	1.07	1.73	2.49	3.28	4.53
CaO	0.91	1.89	3.00	4.54	6.19	8.06
Na_2O	4.41	5.11	5.09	5.67	5.65	5.29
K_2O	5.20	5.12	4.87	4.42	3.84	3.09
Experiment AP-3						
x (μm)	-481	-33	-7	20	52	974
SiO_2	73.02	69.99	66.16	62.28	58.09	54.12
TiO_2	0.13	0.19	0.25	0.38	0.60	0.76
Al_2O_3	13.65	12.98	13.57	14.73	15.48	15.99
FeO_T	2.21	3.04	4.60	5.10	6.74	8.05
MgO	0.26	1.33	1.83	2.62	3.43	4.48
CaO	1.02	2.22	3.50	4.80	6.31	8.20
Na_2O	4.36	5.13	5.22	5.67	5.44	5.19
K_2O	5.35	5.11	4.86	4.42	3.92	3.22
Experiment AP-4						
x (μm)	-1008	-76	-25	38	151	1941
SiO_2	73.11	69.92	66.25	62.43	58.02	54.26
TiO_2	0.10	0.16	0.31	0.40	0.65	0.73
Al_2O_3	13.64	13.26	13.82	14.85	15.54	16.11
FeO_T	2.17	2.91	4.23	5.38	6.66	8.20
MgO	0.27	1.33	1.68	2.49	3.50	4.49
CaO	1.05	2.27	3.76	4.82	6.60	8.27
Na_2O	4.33	5.10	5.18	5.24	5.02	4.79
K_2O	5.34	5.05	4.78	4.39	4.02	3.16

This is a preprint, the final version is subject to change, of the American Mineralogist (MSA)
Cite as Authors (Year) Title. American Mineralogist, in press.
DOI: https://doi.org/10.2138/am-2019-6997

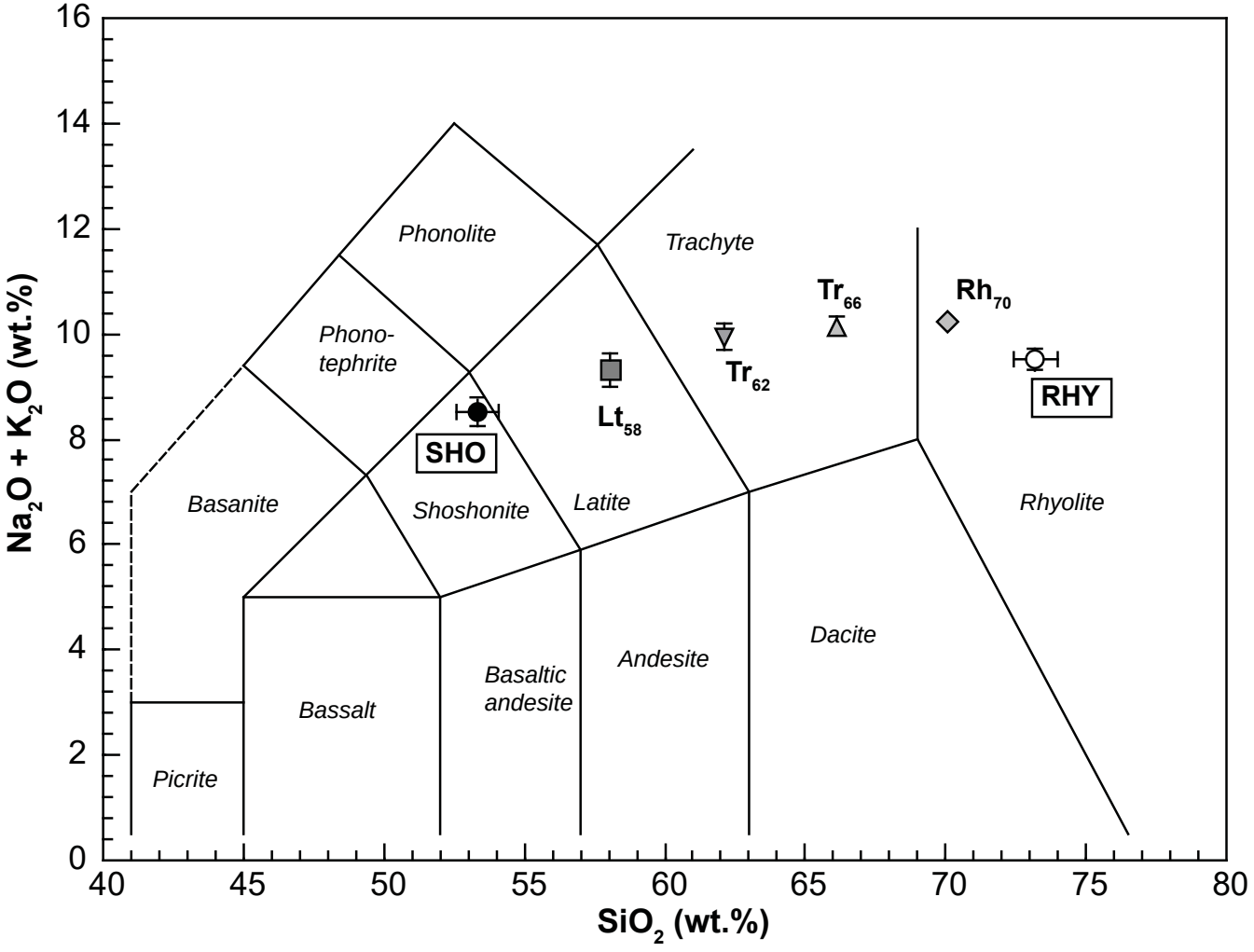

Figure 1

This is a preprint, the final version is subject to change, of the American Mineralogist (MSA)
Cite as Authors (Year) Title. American Mineralogist, in press.
DOI: https://doi.org/10.2138/am-2019-6997

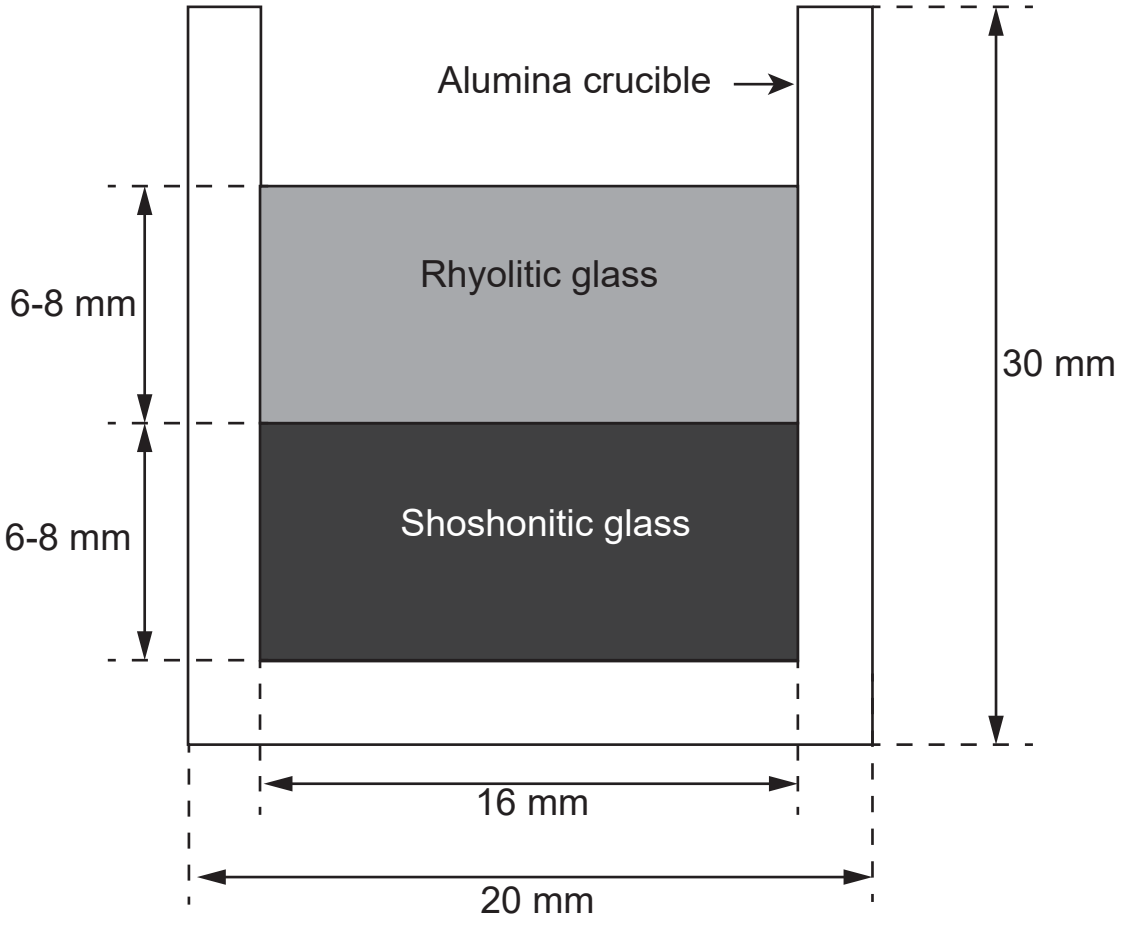

Figure 2

This is a preprint, the final version is subject to change, of the American Mineralogist (MSA)
Cite as Authors (Year) Title. American Mineralogist, in press.
DOI: https://doi.org/10.2138/am-2019-6997

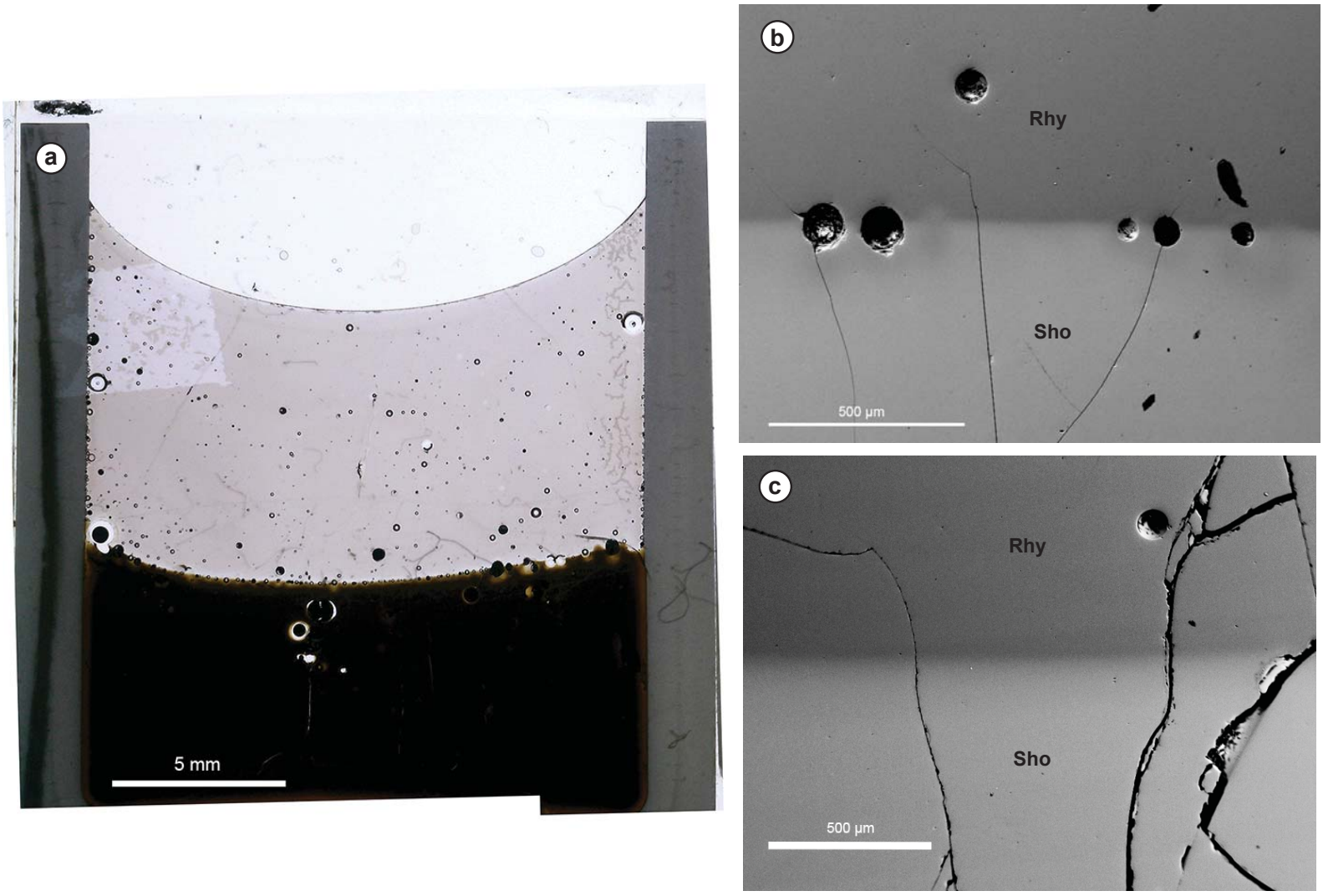

Figure 3

This is a preprint, the final version is subject to change, of the American Mineralogist (MSA)
Cite as Authors (Year) Title. American Mineralogist, in press.
DOI: https://doi.org/10.2138/am-2019-6997

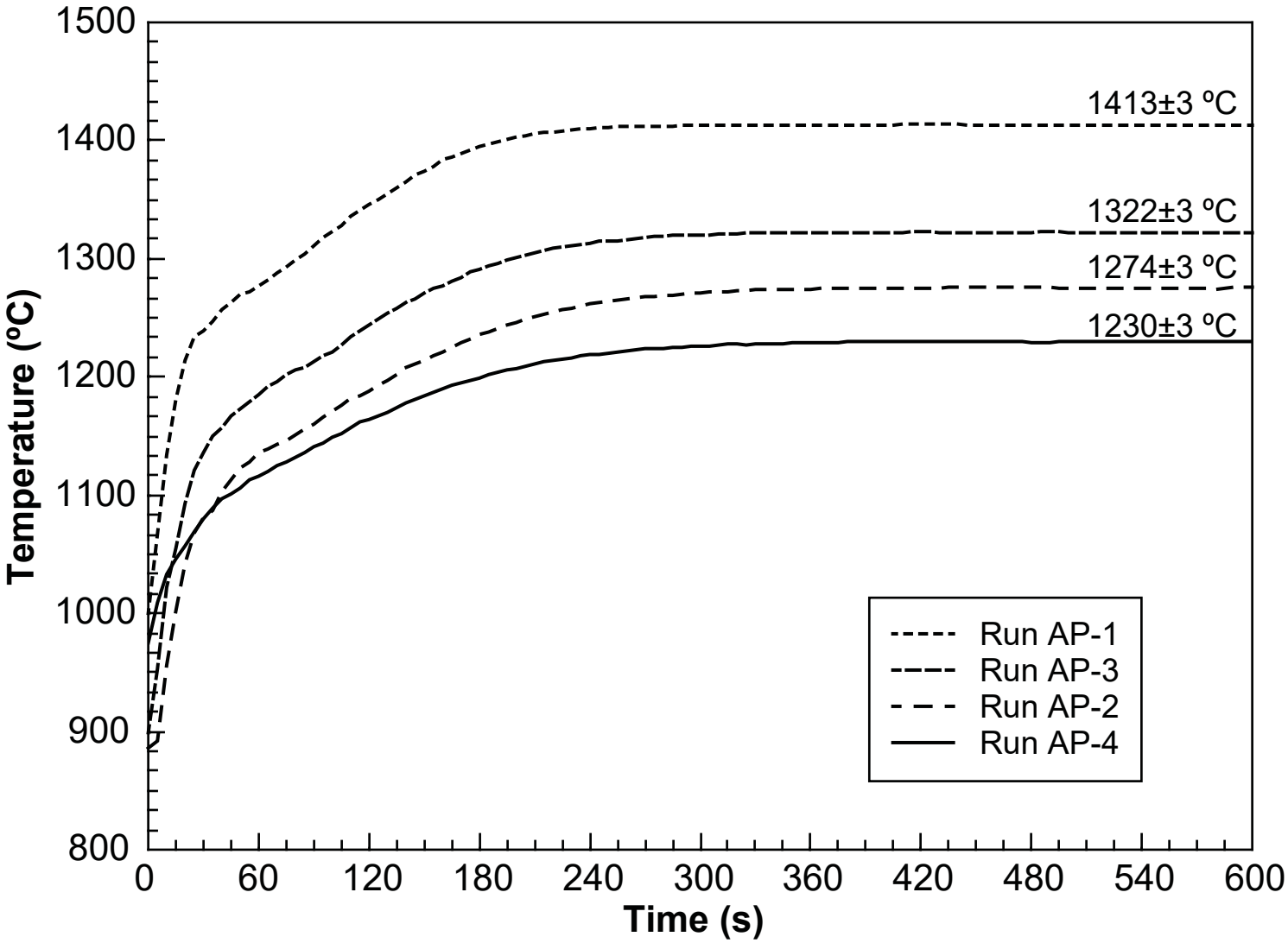

Figure 4

This is a preprint, the final version is subject to change, of the American Mineralogist (MSA)
Cite as Authors (Year) Title. American Mineralogist, in press.
DOI: https://doi.org/10.2138/am-2019-6997

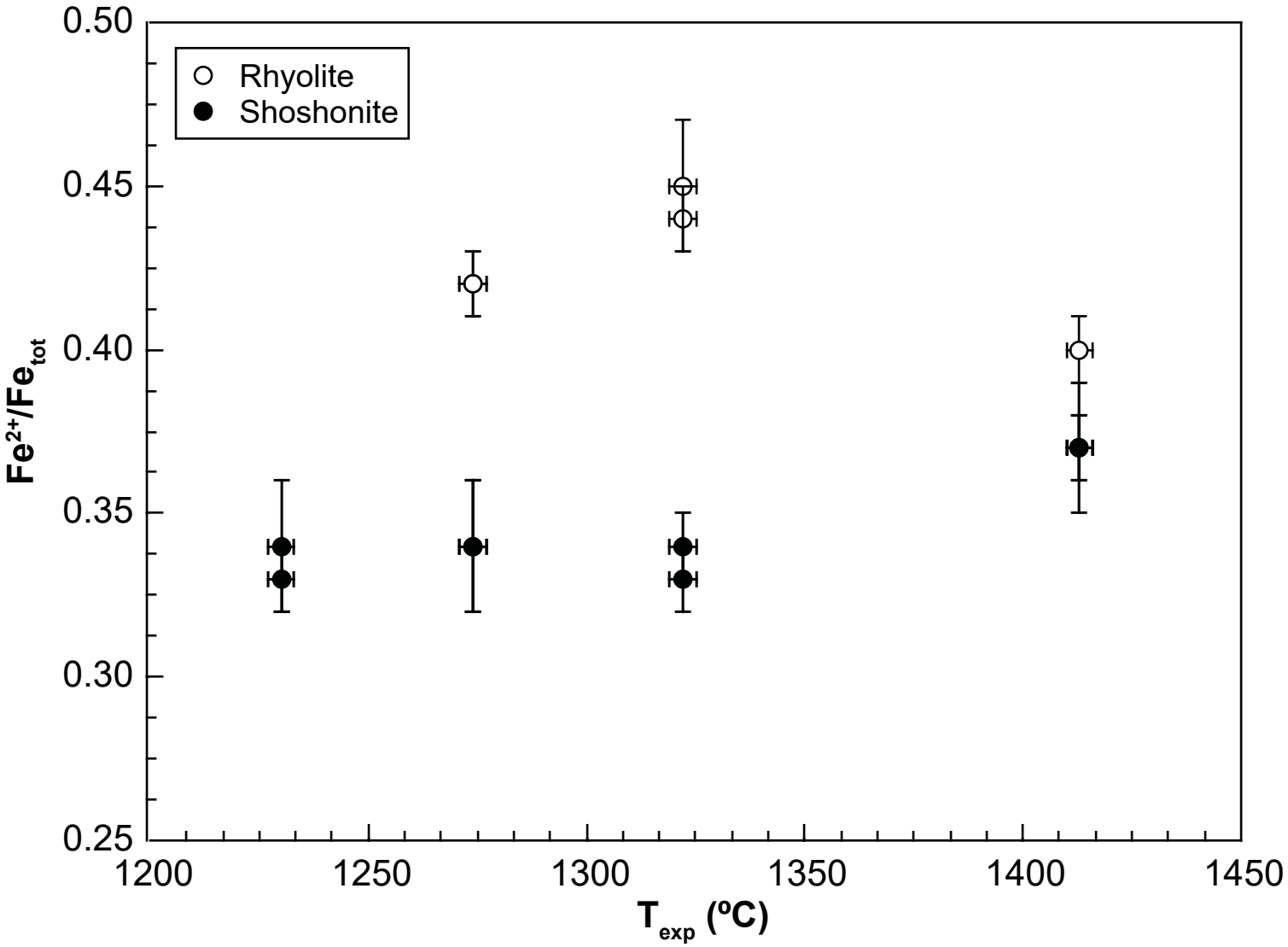

Figure 5

This is a preprint, the final version is subject to change, of the American Mineralogist (MSA)
Cite as Authors (Year) Title. American Mineralogist, in press.
DOI: https://doi.org/10.2138/am-2019-6997

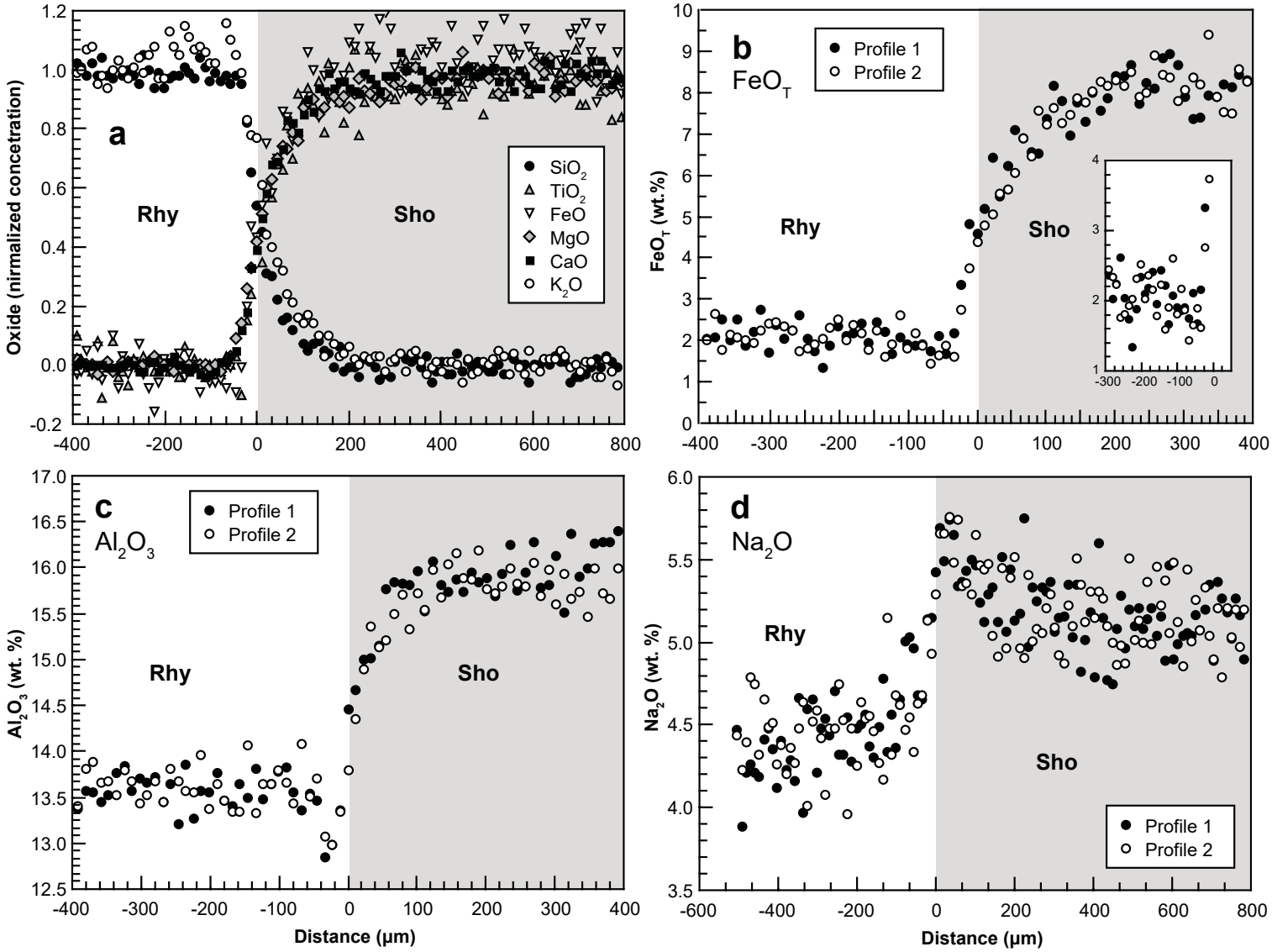

Figure 6

This is a preprint, the final version is subject to change, of the American Mineralogist (MSA)
Cite as Authors (Year) Title. American Mineralogist, in press.
DOI: https://doi.org/10.2138/am-2019-6997

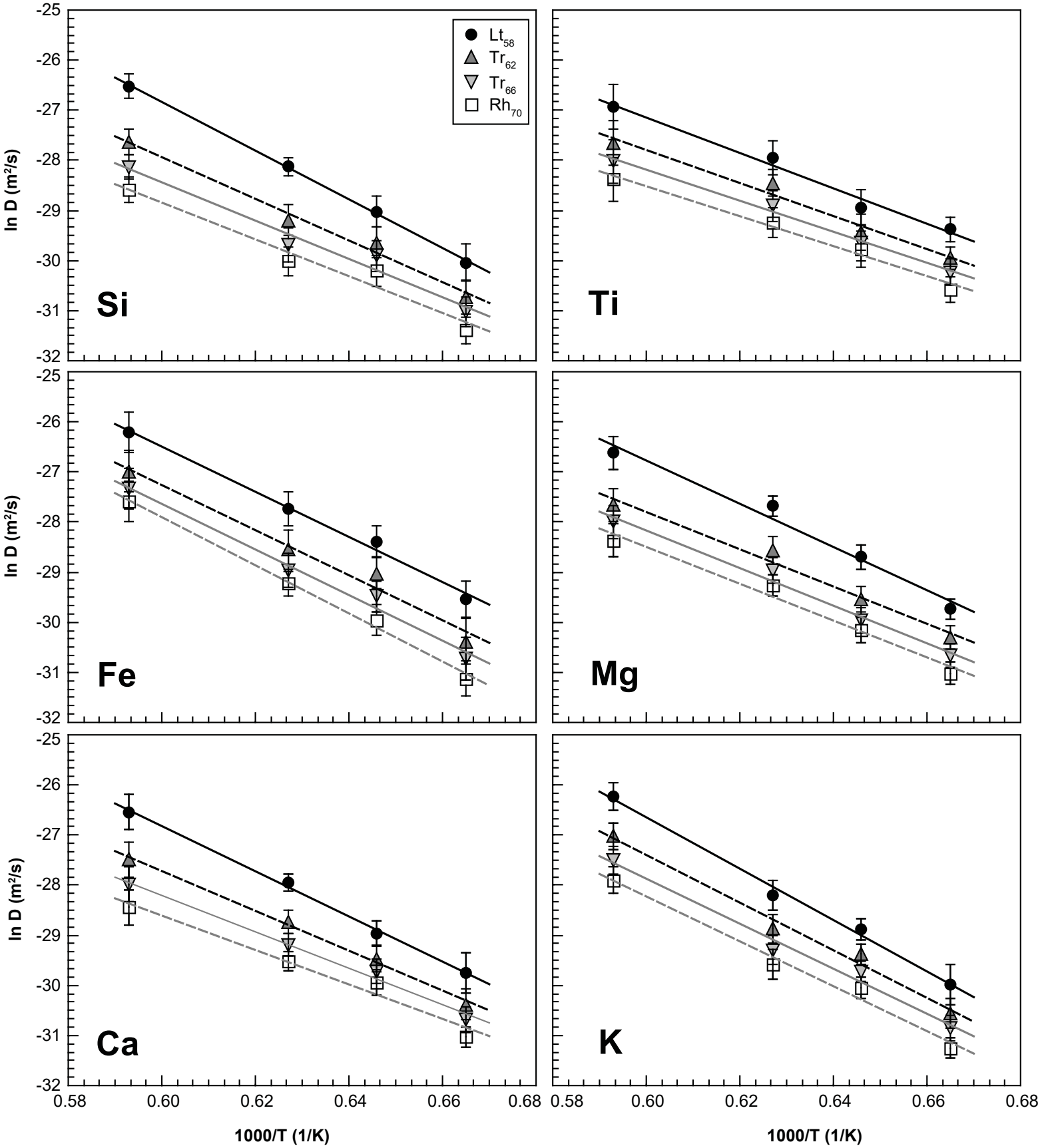

Figure 7

This is a preprint, the final version is subject to change, of the American Mineralogist (MSA)
Cite as Authors (Year) Title. American Mineralogist, in press.
DOI: https://doi.org/10.2138/am-2019-6997

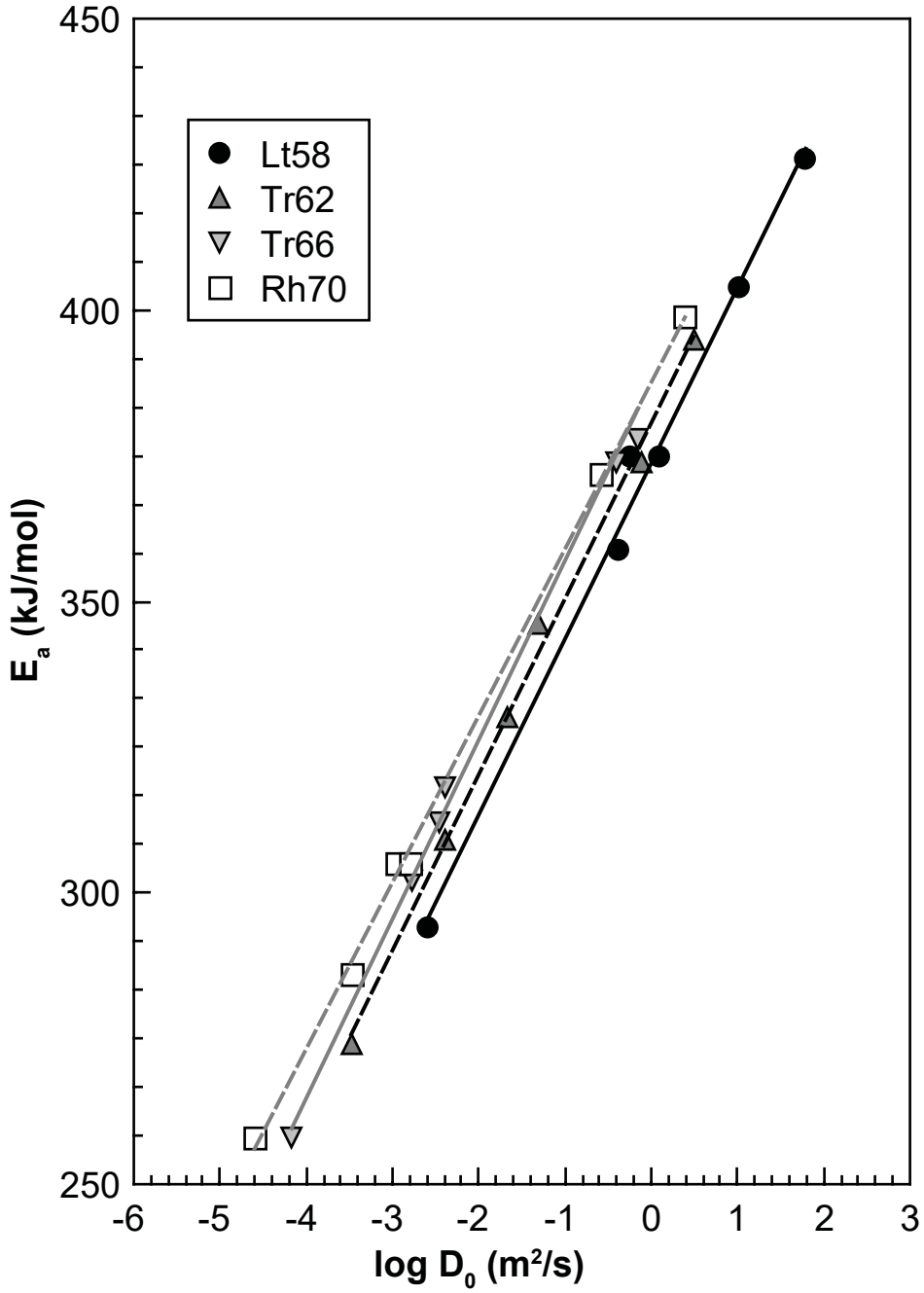

Figure 8

This is a preprint, the final version is subject to change, of the American Mineralogist (MSA)
Cite as Authors (Year) Title. American Mineralogist, in press.
DOI: https://doi.org/10.2138/am-2019-6997

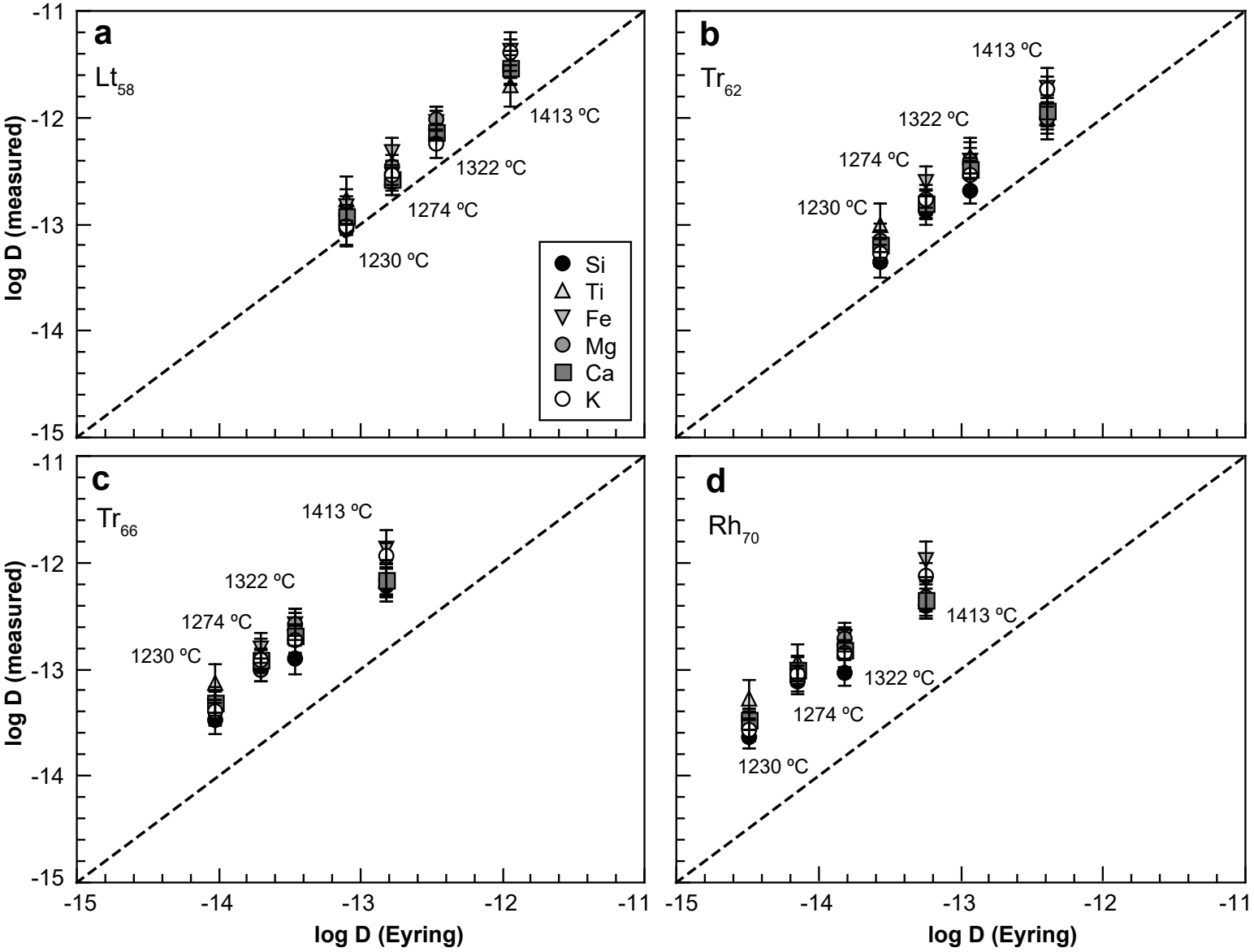

Figure 9

This is a preprint, the final version is subject to change, of the American Mineralogist (MSA)
Cite as Authors (Year) Title. American Mineralogist, in press.
DOI: https://doi.org/10.2138/am-2019-6997